Interpretation of the THz-THz-Raman Spectrum of Bromoform

Published as part of The Journal of Physical Chemistry virtual special issue "Pacific Conference on Spectroscopy and Dynamics".
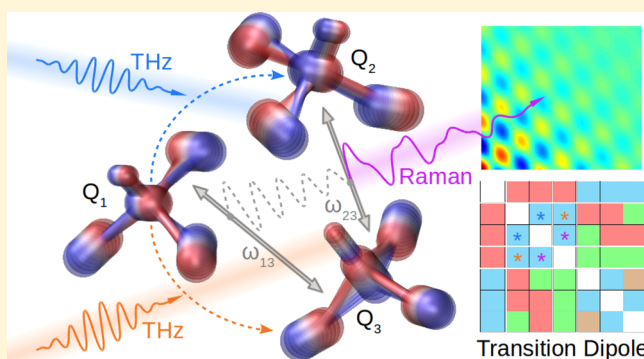
Ioan B. Magdău,[†] Griffin J. Mead,[†] Geoffrey A. Blake,*[,†,‡] and Thomas F. Miller, III*[,†] [ORCID]

[†]Division of Chemistry & Chemical Engineering, California Institute of Technology, Pasadena, California 91125, United States
[‡]Division of Geological & Planetary Sciences, California Institute of Technology, Pasadena, California 91125, United States

ABSTRACT: Nonlinear THz-THz-Raman (TTR) liquid spectroscopy offers new possibilities for studying and understanding condensed-phase chemical dynamics. Although TTR spectra carry rich information about the systems under study, the response is encoded in a three-point correlation function comprising of both dipole and polarizability elements. Theoretical methods are necessary for the interpretation of the experimental results. In this work, we study the liquid-phase dynamics of bromoform, a polarizable molecule with a strong TTR response. Previous work based on reduced density matrix (RDM) simulations suggests that unusually large multiquanta dipole matrix elements are needed to understand the measured spectrum of bromoform.

Here, we demonstrate that a self-consistent definition of the time coordinates with respect to the reference pulse leads to a simplified experimental spectrum. Furthermore, we analytically derive a parametrization for the RDM model by integrating the dipole and polarizability elements to the 4th order in the normal modes, and we enforce inversion symmetry in the calculations by numerically canceling the components of the response that are even with respect to the field. The resulting analysis eliminates the need to invoke large multiquanta dipole matrix elements to fit the experimental spectrum; instead, the experimental spectrum is recovered using RDM simulations with dipole matrix parameters that are in agreement with independent ab initio calculations. The fundamental interpretation of the TTR signatures in terms of coupled intramolecular vibrational modes remains unchanged from the previous work.

1. INTRODUCTION

Two dimensional time-resolved spectroscopy encompasses techniques in which a sequence of three or four coherent laser pulses is used to measure the response of the system with respect to two time delays. The direct Fourier transform of this response corresponds to a frequency—frequency correlation function that carries rich information about the anharmonicity, coupling, and nonlinearity of the vibrational and electronic states. These characteristics elucidate the underlying dynamics and various energy dissipation processes, such as homogeneous and inhomogeneous broadening.

Each laser pulse in the sequence creates or destroys coherences via one of two physical processes: optical absorption (1st order in the field interaction) or Raman scattering (2nd order in the field interaction). These processes can take place in the visible (VIS) regime probing electronic states, the infrared (IR) regime measuring high frequency intramolecular vibrational modes, or the terahertz (THz) regime probing low-frequency modes, such as lattice phonons or intermolecular vibrations. Combination of these various laser pulses leads to a range of different spectroscopic methods, such as 2D-IR, 2D-VIS, VIS-IR, 2D-Raman, etc., each with its own applicability.

2D-IR spectroscopy was one of the first methods used to investigate the vibrational properties of liquids, and it has helped address topics that include structural fluctuations in water,[1−4] proton shuttling in acidic solutions,[5,6] and protein dynamics.[7−9] While 2D-IR has proven useful for studying high-frequency vibrational modes, there is strong motivation to extend multidimensional spectroscopy to the low-frequency regime. Important physical chemical processes, such as collective solvent motions[10−12] and dynamics of large biomolecules,[13−15] are driven by processes that takes place in the THz range. The first method developed to study liquids in the THz domain was 2D-Raman spectroscopy.[16] This method is 5th order in the laser field, and it has been shown to suffer from cascading effects where the 5th order response is plagued by contributions from higher intensity 3rd order processes.[17] It is only with difficulty that these cascaded processes were overcome to yield the true 5th order 2D Raman response.[18,19]

The advent of powerful THz sources[20,21] has enabled 3rd order hybrid spectroscopic techniques, in which one or two of

the 2nd order Raman processes are replaced by 1st order THz absorption: RTT, TRT, and TTR.[22] The RTT and TRT methods measure a THz emission and were first employed to study water and aqueous solutions.[12,23−25] TTR builds upon the pulse-detection methods developed in THz-Kerr-effect spectroscopy,[26,27] which has been successfully applied in both polar and nonpolar liquids.[28,29] The TTR approach was recently developed in our group[30,31] and used to measure the 3rd order nonlinear response of liquid bromoform[32] ($CHBr_3$), carbon tetrachloride (CCl_4) and dibromodichloromethane (CBr_2Cl_2). These halogen liquids are ideal test systems for TTR because they exhibit intramolecular modes in the THz frequency regime and are Raman-active due to their strong polarizability.[33]

All three Raman-THz hybrid methods (i.e., RTT, TRT, and TTR) are complementary and measure different correlation functions involving the dipole and polarizability surfaces. These responses carry rich information about the systems under study, including the nonlinearity of the dipole and polarizability surfaces and the anharmonicity and mechanical coupling of the various vibrational motions. However, this information is encoded in complex, three-point correlation functions that must be disentangled with the aid of theoretical and computational methods.[30,31,34−48] This problem of interpretation is further complicated by the number of vibrational states that need to be considered. Whereas infrared-active modes are usually in their vibrational ground state at room temperature and typically only involve single excitations upon illumination, THz-active modes can be thermally excited at room temperature, and multiple transitions between the different states are possible.

In our previous work,[31] we developed a reduced density matrix (RDM) model to understand the TTR spectrum in liquid bromoform. When the parameters for the nonlinear dipole elements in the RDM model were fit to best reproduce the experimental TTR signal, it was found that they assumed unexpectedly large values that did not agree with our accompanying ab initio electronic structure calculations. Here, we reconcile this apparent inconsistency by developing a more complete description of the TTR spectra from both the theoretical and experimental perspective.

2. METHOD DEVELOPMENT

We begin by reviewing the RDM model of refs 30 and 31. In the section 2.1, we describe the time-coordinate transformation necessary to reinterpret the experimental spectrum. In sections 2.2 and 2.3, we explain the development of a new RDM model that fully accounts for the liquid symmetry and the symmetries of the dipole and polarizability matrices to 4th order in the normal modes.

In RDM, we propagate the reduced density matrix $\rho(t)$ for a single bromoform molecule by solving the Liouville−von Neumann equation[49]

$$\frac{\partial \rho(t)}{\partial t} = -\frac{i}{\hbar}[H(t), \rho(t)] - \Gamma\rho(t) \tag{1}$$

where Γ is a constant phenomenological relaxation matrix that accounts for the interaction with the bath by population relaxation ($\Gamma_{nn} = \frac{1}{\tau_1}$, where $\tau_1 = 100$ fs) and coherence dephasing ($\Gamma_{nm} = \frac{1}{\tau_2}$, where $\tau_2 = 2$ ps). We tested longer population relaxation times up to 10 ns, and we found no change in the computed TTR response.

The time-varying Hamiltonian, $H(t)$, describes interactions of the system with the THz fields

$$H(t; t_1) = H - M \cdot E_T(t) - M \cdot E_T(t - t_1) \tag{2}$$

where $E_T(t)$ is the experimentally measured pulse shape,[31] H is the system Hamiltonian, and M is the transition dipole matrix. Using $E_T(t)$ in the simulation, instead of a simple delta function $E\delta(t)$ ensures that the computed spectrum is in fact the molecular response convoluted with the instrument response function (IRF) and can be directly compared to the raw experimental data.

We propagate eq 1 forward in time by numerical integration, noting that the mixed central-forward scheme provides good numerical stability

$$\rho(t + dt; t_1) = \rho(t - dt; t_1) - \frac{2i}{\hbar}[H(t; t_1), \rho(t; t_1)]dt$$
$$- 2\Gamma\rho(t - dt; t_1)dt \tag{3}$$

where the commutator is discretized by central difference, which preserves time reversibility, and the phenomenological dissipation is discretized by forward difference. We, then, calculate the TTR signal as the field emitted by the final Raman process

$$S^{Th}(t_2; t_1) = \Re(\text{Tr}(\Pi \cdot \rho(t_2; t_1)P)) \tag{4}$$

where Π is the transition polarizability, another important model parameter, and P is a matrix with elements

$$P_{nm} = i, \ P_{mn} = -i, \text{ and } P_{nn} = 1 \tag{5}$$

P ensures that the signal is emitted 90° out-of-phase with respect to the induced polarization.[49]

We compute the frequency response from the absolute value of the Fourier transform, normalized to its maximum value,

$$\tilde{S}^{Th}(f_2; f_1) = |\text{FT}(S^{Th}(t_2; t_1)| \tag{6}$$

For a given realization of parameters in H, M, and P, comparison of the simulated and experimental TTR signals is made via the logarithmic error function:

$$\delta = \iint df^2 [\log(\tilde{S}^{Ex}(f_2; f_1)) - \log(\tilde{S}^{Th}(f_2; f_1))]^2 \tag{7}$$

We fit the RDM model by minimizing δ with respect to H, M, and P, subject to L_2-norm regularization. Specifically, we minimize

$$\Delta = \delta + \lambda(h_i^2 + \mu_j^2 + \alpha_k^2) \tag{8}$$

where h_i, μ_i, and α_i are the parameters of the Hamiltonian $H = H(h_i)$, transition dipole $M = M(\mu_i)$, and transition polarizability $\Pi = \Pi(\alpha_i)$ operators.

We note that eq 1 only accounts for Markovian dissipative processes. This description may of course be extended to include more complex relaxation phenomena, such as coherence and population transfer in the context of non-Markovian dynamics,[50−52] which have been shown to be important in some liquids.

2.1. Interpreting the Experimental Data. The experimental setup[30] consists of two THz pump pulses, THz_1 and THz_2, which are polarized along the Y and X directions and separated by a time delay, $t_1 = t_{THz_1} - t_{THz_2}$. A near-infrared (NIR) optical probe, polarized along X, induces a Y-polarized Raman response from the system at time delay $t_2 = t_{NIR} - t_{THz_1}$. Because of the symmetry of the third-order response, a Raman

signal is only detected after the second THz pump has interacted with the system. Experimentally, t_1 is scanned by changing the path length that the THz_2 field travels, while the THz_1 field remains fixed in time. A consequence of this design is that the third-order response will occur at $t_2 = 0$, when THz_1 is the second field interaction ($t_1 > 0$), but at a time $t_2 = t_1$, when THz_2 is the second interaction ($t_1 < 0$). Qualitatively, a diagonally skewed TTR response is observed in the $t_1 < 0$ region. This must be properly accounted for in the interpretation of the spectrum.

To illustrate the importance of correctly including this skew in the analysis, we consider how a Liouville pathway in a generic system, composed of two vibrational modes, changes when evaluated at $t_1 > 0$ and $t_1 < 0$. In Figure 1a, we label these two
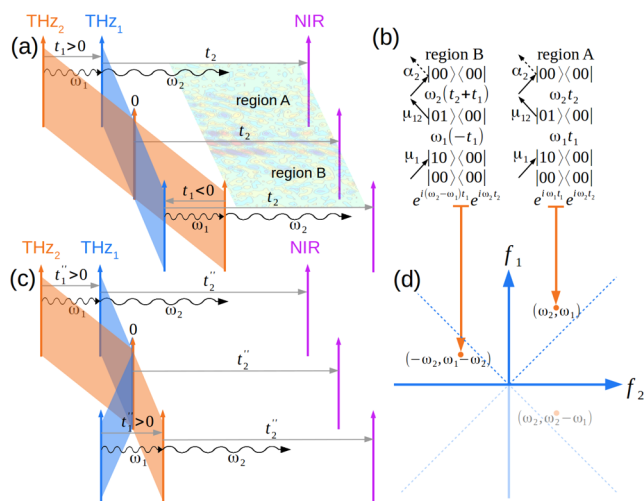

Figure 1. Illustration of the THz pump pulses switching time ordering and the resulting impact on various spectral features. Panel a shows a schematic of the experimental setup and the definition of time coordinates t_1 and t_2 in the two regions of response, A and B, corresponding to the pulse sequence THz_2-THz_1-NIR and THz_1-THz_2-NIR, respectively. Panel b illustrates a generic Liouville pathway represented by two distinct Feynman diagrams that feature different oscillatory phases in the portions of response A and B, as a consequence of mixing the time coordinates. These two Feynman diagrams which represent the same physical process manifest as two distinct peaks in the Fourier representation of the response: panel d. Finally, panel c illustrates the transformed time coordinates t_1'' and t_2'' which fix this issue.

regions A and B, corresponding to pulse ordering THz_2-THz_1-NIR ($t_1 > 0$) and THz_1·THz_2-NIR ($t_1 < 0$), respectively. When the pathway is sampled in region A of the response, the first THz pulse excites coherence $|10\rangle\langle 00|$, which oscillates at frequency ω_1 and acquires phase $e^{i\omega_1 t_1}$, while the second THz pulse switches the coherence to $|01\rangle\langle 00|$ which oscillates at frequency ω_2 and acquires phase $e^{i\omega_2 t_2}$. Overall, this physical process generates a signal that is proportional to $e^{i\omega_1 t_1}e^{i\omega_2 t_2}$. The same pathway, when sampled in region B, generates a signal that is proportional to $e^{-i\omega_1 t_1}e^{i\omega_2(t_2+t_1)}$, or rearranging, $e^{i(\omega_2-\omega_1)t_1}e^{i\omega_2 t_2}$. Hence, taking the Fourier transform of the full t_1 domain (including both regions A and B) results in two distinct peaks at (ω_2, ω_1) and $(\omega_2, \omega_2 - \omega_1) = (-\omega_2, \omega_1 - \omega_2)$ that otherwise represent the same physical process. This is undesirable and creates the opportunity for misinterpreting the TTR spectrum.

To ensure that each physical process is represented by a single distinct peak, we perform a coordinate transformation of the

time response before computing the frequency response by FT. This transformation consists of skewing the response along t_2

$$(t_2', t_1') = \begin{cases} (t_2, t_1), & \text{region A} \\ (t_2 + t_1, t_1), & \text{region B} \end{cases} \quad (9)$$

and then flipping it with respect to t_1

$$(t_2'', t_1'') = \begin{cases} (t_2', t_1') = (t_2, t_1), & \text{region A} \\ (t_2', -t_1') = (t_2 + t_1, -t_1), & \text{region B} \end{cases} \quad (10)$$

as shown in Figure 1(c). With these transformed time coordinates, our illustrative Liouville pathway acquires the same phase factors $e^{i\omega_1 t_1''}e^{i\omega_2 t_2''}$ when sampled in region B as in region A. This transformation simplifies the resulting TTR spectrum and eliminates the appearance of redundant peaks.

2.2. Enforcing Inversion Symmetry in the RDM Model. Liquids are isotopic, such that any response function

$$S(E) = \varepsilon_1 E + \varepsilon_2 E^2 + \varepsilon_3 E^3 + \varepsilon_4 E^4 + \dots \quad (11)$$

must obey inversion symmetry with respect to an applied electric field, E. The TTR response must also obey this symmetry

$$S(-E_T, -E_T, -E_{NIR}) = -S(E_T, E_T, E_{NIR}) \quad (12)$$

and requires that even-order contributions to the experimentally observed response must vanish

$$\varepsilon_2 = \varepsilon_4 = \dots = 0 \quad (13)$$

This means that only scattering processes that involve an odd number of photons, not counting the final emission, can generate an experimental TTR signal. In the case of liquid bromoform, the final Raman process is linear and it only involves a one-photon absorption.[31] Therefore, the total number of THz photon interactions must be even and the leading contribution to the TTR signal is 3rd order in the field, involving the absorption of two THz photons and one NIR photon. In other words, the TTR response scales linearly with each of the THz fields.

Figure 2b lists all possible 3rd order interactions in which two THz photons are involved: 1−1−1, 2−0−1 and 0−2−1. The TTR experiment further isolates the desired 1−1−1 response by employing differential chopping.[30] In the RDM simulations, we implement differential chopping by separating the 1D responses S_2^{Th} and S_1^{Th} from the total response S^{Th}, as illustrated in Figure 2a. We compute these individual responses by propagating the dynamics under the partial Hamiltonians

$$H_2(t; t_1) = H - M \cdot E_T(t) \text{ and}$$

$$H_1(t; t_1) = H - M \cdot E_T(t - t_1) \quad (14)$$

This simulation procedure removes the unwanted field interactions, shaded purple in Figure 2, from the 3rd response. However, the RDM simulated response[30,31] also includes 4th order interactions, unlike the experiment where even order processes vanish due to the symmetry of the liquid, as explained above.

It is found that for the simulated TTR response, 4th order contributions can be comparable in magnitude to 3rd order ones because the latter require at least one nonlinear dipole interaction while the former do not. [To prove that all 3rd order TTR pathways require a nonlinear dipole interaction, consider a 3rd order Liouville pathway which starts from a
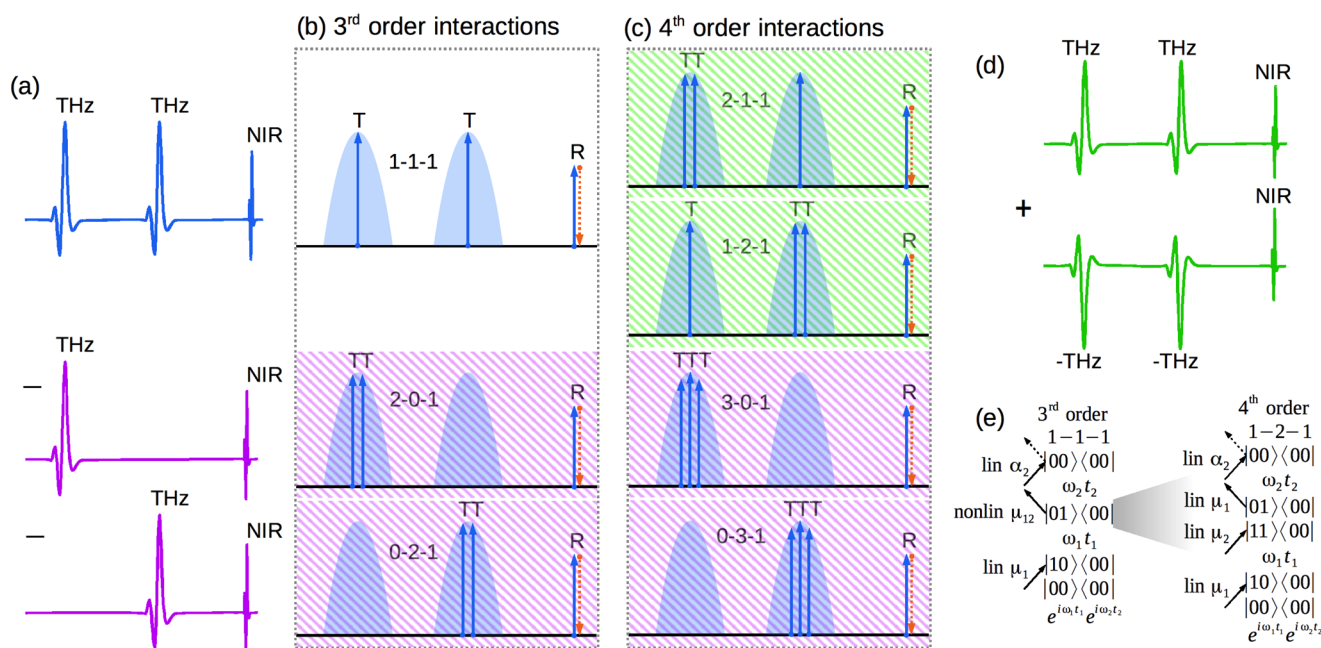
Figure 2. Differential chopping and enforced inversion symmetry remove unwanted responses from the spectrum generated via RDM. Panel a schematically illustrates differential chopping, while panel d shows how we enforce inversion symmetry. Panels b and c list all 3rd and 4th order field interactions manifested in the RDM, from which only the $1-1-1$ process is sampled experimentally. Shaded in purple are the processes removed by differential chopping, and in green the processes removed by enforcing inversion symmetry. Panel e exemplifies two similar Liouville pathways of 3rd and 4th order, in which the transfer of coherence from $|10\rangle\langle00|$ to $|01\rangle\langle00|$ takes place via one nonlinear dipole interaction in the former and two linear dipole interactions in the latter.

generic population state $|a\rangle\langle a|$. Interaction of the system with the first THz pulse changes the excitation state of the bra or ket of the density matrix by n quanta to a $|a + n\rangle\langle a|$ coherence. Then, upon a second THz interaction, the system changes to either $|a + n + m\rangle\langle a|$ or $|a + n\rangle\langle a + m|$. Since the final Raman interaction only changes the system by a single quantum,[31] and since all pathways must end in a population state, it follows that either $|n + m| = 1$ or $|n - m| = 1$. All paths involving $n = 0$ or $m = 0$ are removed by differential chopping, and therefore all surviving diagrams have both nonzero n and m. As a result, at least one of the THz processes exchanges more than one quantum with the systems, and it is strictly nonlinear.] For instance, in Figure 2e, we compare two similar pathways of 3rd and 4th order. In the 3rd order process, the two-quanta excitation from $|10\rangle$ to $|01\rangle$ is achieved by a single photon interacting with a nonlinear dipole element and has a scattering amplitude proportional to

$$\sigma_{3rd} \propto \langle 10 \left| \frac{\partial^2 M}{\partial Q_1 \partial Q_2} \right| 01 \rangle E_T \qquad (15)$$

Meanwhile, in the 4th order process, the same excitation is achieved by two consecutive photons acting on the linear dipole via an intermediate state

$$\sigma_{4th} \propto \langle 10 \left| \frac{\partial M}{\partial Q_2} \right| 11 \rangle \langle 11 \left| \frac{\partial M}{\partial Q_1} \right| 01 \rangle E_T^2 \qquad (16)$$

For large THz fields, this "all-linear" 4th order contribution can become larger than the 3rd order one if the system has small dipole nonlinearities, such that

$$\frac{\partial^2 M}{\partial Q_1 \partial Q_2} \lesssim E_T \frac{\partial M}{\partial Q_2} \frac{\partial M}{\partial Q_1} \qquad (17)$$

To address this issue, 4th order contributions to the simulated RDM response must be explicitly removed. We achieve this by simulating both the response to positive THz fields and negative THz fields and then summing the two contributions as illustrated in Figure 2d

$$S^{Th} = S^{Th}(E_T, E_T) + S^{Th}(-E_T, -E_T) \qquad (18)$$

This procedure ensures that the final response function is odd with respect to the overall field and that the 4th order contributions, shaded green in Figure 2c, vanish. As a result, the simulated TTR spectrum correctly reflects the inversion symmetry of the liquid state and can be compared directly to the experimental spectrum.

2.3. The Hamiltonian, Dipole, and Polarizability Surfaces. The bromoform molecule has three vibrational degrees of freedom in the terahertz regime: two degenerate C−Br bending modes at 4.7 THz, Q_1 and Q_2, and a symmetric umbrella mode at 6.6 THz, Q_3.[53] Figure 3a illustrates these motions and provides an energy-level diagram with the number of quanta in each mode indicated, using notation $|Q_1 Q_2 Q_3\rangle$. In typical 2D-IR spectroscopy applications at room temperature, only the ground and first-excited state of each mode are involved. TTR spectroscopy probes modes that are low in energy, such that even at room temperature ($kT \approx 6.2$ THz), it is necessary to consider thermally accessible excited states. In the current study, the bandwidth of the THz pulse covers BW ≈ 8 THz of energy, such that all states below $kT + BW \lesssim 14.2$ THz should be considered. The highest energy state that is included in our model is the quadruplet $Q_1 \otimes Q_2$, amounting to three quanta of energy in the degenerate mode (3×4.7 THz = 14.1 THz).
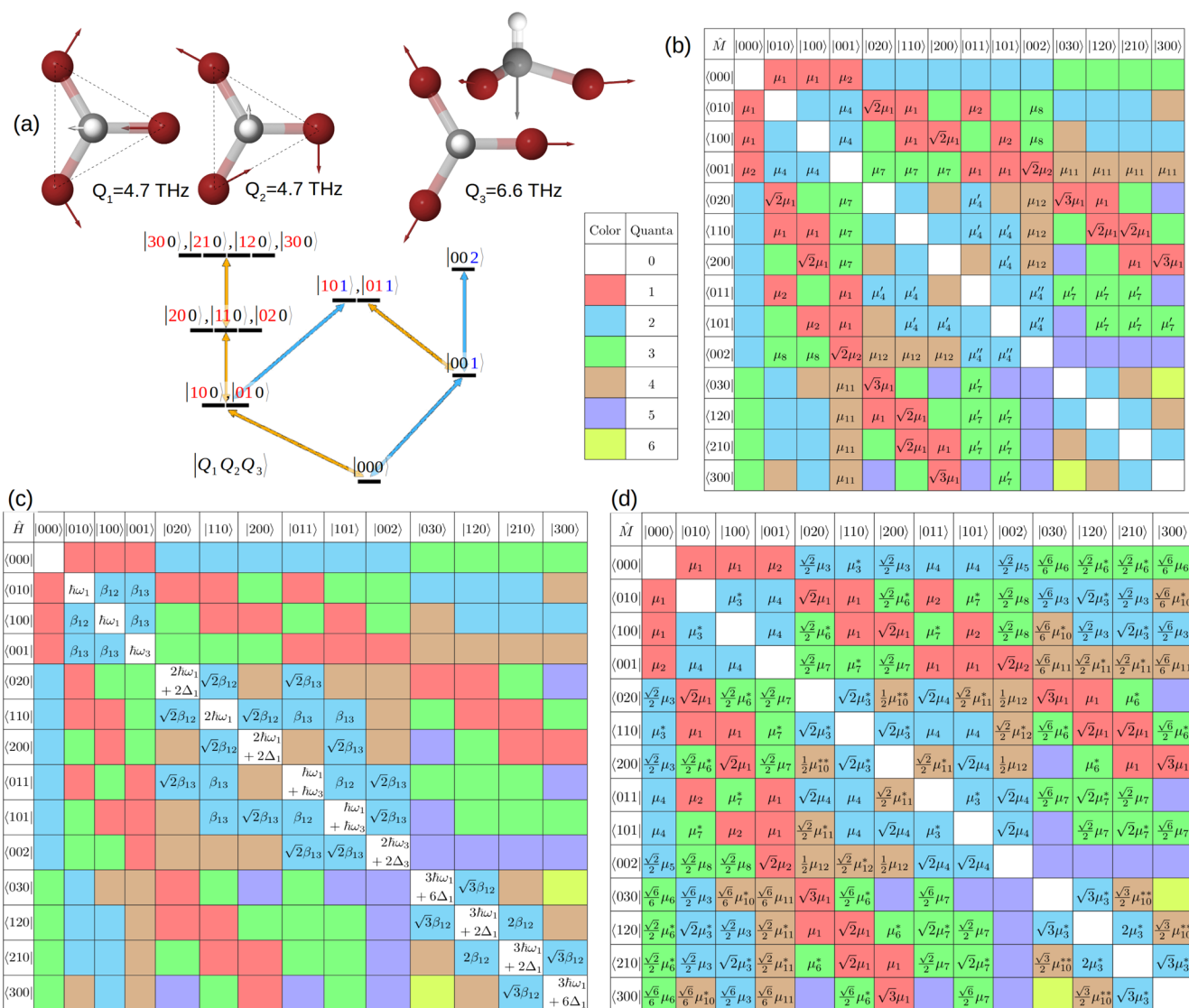
Figure 3. Panel a shows the low energy normal modes of the bromoform molecule: the degenerate "C−Br bending modes" Q_1 and Q_2 at 4.7 THz and the "umbrella mode" Q_3 at 6.6 THz. The panel also shows the corresponding quantum states labeled $|Q_1Q_2Q_3\rangle$ that we use to describe these normal modes. The double arrow indicates all possible 1-quantum transitions between these states. Panel b shows the parametrization of the transition dipole moment ($\hat{M}$) used in ref 31. The color assigned to each matrix element corresponds to the number of quanta involved in that transition as summarized in the inset table. Elements that appear empty are fixed to zero. Panels c and d illustrate the Hamiltonian ($\hat{H}$) and transition dipole ($\hat{M}$) in the current RDM model, as derived by integrating eqs 22 and 23. Notice that in this work the dipole is fully parametrized to the 4th order and only transition matrix elements higher than 4th order are set to zero.

The calculated TTR spectrum depends on the parametrization of $H = H(h_i)$, $M = M(\mu_i)$, and $\Pi = \Pi(\alpha_i)$. In the RDM model of ref 31, we employed a harmonic Hamiltonian

$$\hat{H} = \hbar\omega_1(\hat{a}_1^\dagger \hat{a}_1 + \hat{a}_2^\dagger \hat{a}_2) + \hbar\omega_3 \hat{a}_3^\dagger \hat{a}_3 \qquad (19)$$

the parameters for which were fixed to the linear absorption experimental spectrum, and a transition dipole of the form

$$\hat{M} = \mu_1(\hat{Q}_1 + \hat{Q}_2) + \mu_2 \hat{Q}_3 + \hat{M}_{2q}(\mu_4, \mu_4', \mu_4'')$$
$$+ \hat{M}_{3q}(\mu_7, \mu_7', \mu_8) + \hat{M}_{4q}(\mu_{11}, \mu_{12}) \qquad (20)$$

where $\hat{M}_{nq}$ represent the nonlinear blocks of the dipole operator comprised of n-quanta ($n > 1$) transitions, which were determined by fitting to the nonlinear TTR experimental spectrum. The $\hat{Q}_i$ are nondimensional normal modes which can

be expressed in terms of the creation and annihilation operators $\hat{a}_i^\dagger$ and $\hat{a}_i$

$$\hat{Q}_i = \sqrt{\frac{2m_i\omega_i}{\hbar}}\,\hat{q}_i = \hat{a}_i^\dagger + \hat{a}_i \qquad (21)$$

Combining eqs 21 and 20 and integrating the linear part of the dipole in the $|Q_1Q_2Q_3\rangle$ basis leads to the matrix parametrization of ref 31 (Figure 3b).

In this work, we develop a more comprehensive model for the Hamiltonian, which includes the anharmonicity Δ_i of the single molecule normal modes, as well as mode coupling β_{ij} originating from the condensed-phase environment. We employ a quantum-conserving Hamiltonian of the form
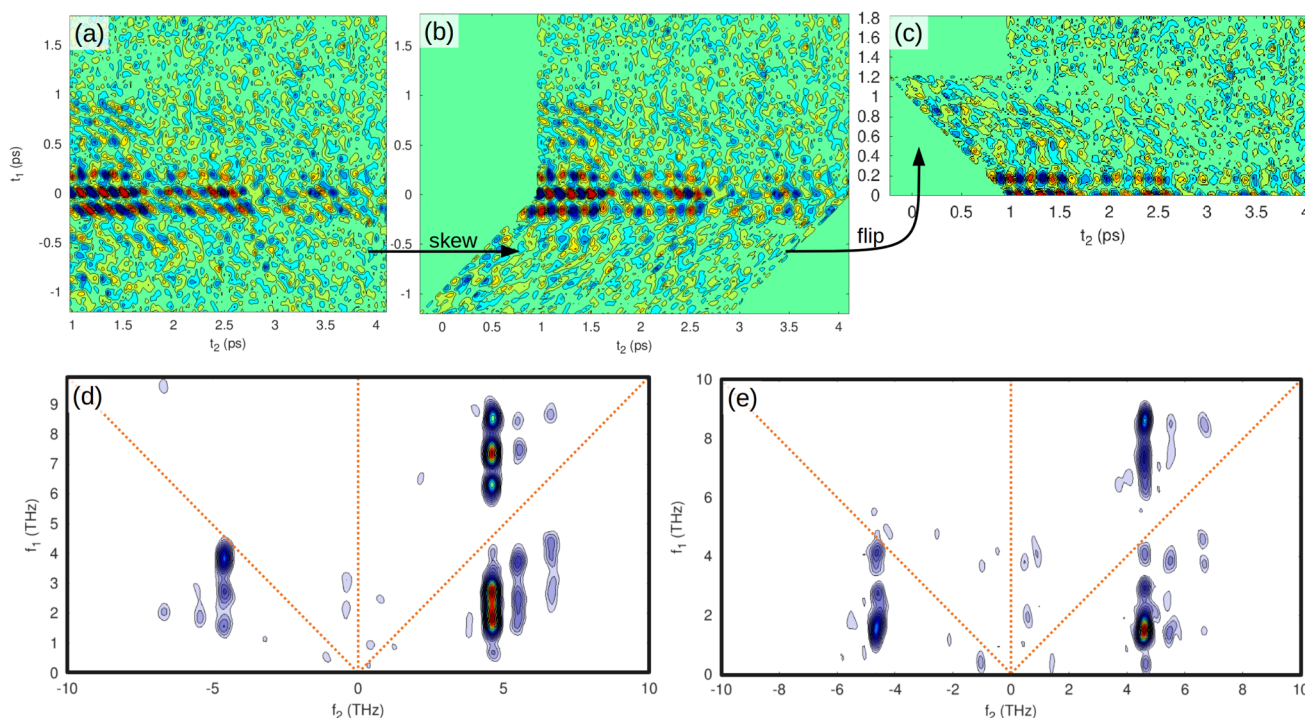
Figure 4. Illustration of the effect of the introduced time-coordinate transformation on the experimental spectrum. Panels a−c show how the time transformation (skew and flip) alters the response in time domain. Panel a corresponds to the initial coordinates represented schematically in Figure 1a, while panel c to the proposed coordinates represented in Figure 1c. Panels d and e present the Fourier transforms of panels a and c, before and after the time transformation, respectively.

$$\hat{H} = \hbar\omega_1(\hat{a}_1^\dagger\hat{a}_1 + \hat{a}_2^\dagger\hat{a}_2) + \hbar\omega_3\hat{a}_3^\dagger\hat{a}_3 + \beta_{12}(\hat{a}_1^\dagger\hat{a}_2 + \hat{a}_1\hat{a}_2^\dagger)$$
$$+ \beta_{13}(\hat{a}_2^\dagger\hat{a}_3 + \hat{a}_2\hat{a}_3^\dagger + \hat{a}_1^\dagger\hat{a}_3 + \hat{a}_1\hat{a}_3^\dagger)$$
$$+ \Delta_1(\hat{a}_1^{\dagger 2}\hat{a}_1^2 + \hat{a}_2^{\dagger 2}\hat{a}_2^2) + \Delta_3\hat{a}_3^{\dagger 2}\hat{a}_3^2 \tag{22}$$

and integrate it in the $|Q_1Q_2Q_3\rangle$ basis to obtain the matrix representation shown in Figure 3c. Note that the couplings between the doubly degenerate modes $Q_{1,2}$ and mode Q_3 are equivalent and labeled β_{13} in eq 22.

Furthermore, we Taylor expand the dipole operator to 4th order in the normal modes and enforce the $Q_{1,2}$ symmetry by grouping together terms which are invariant to label exchange $(1 \leftrightarrow 2)$

$$\hat{M} = \mu_1(\hat{Q}_1 + \hat{Q}_2) + \mu_2\hat{Q}_3 + \frac{1}{2!}\mu_3(\hat{Q}_1^2 + \hat{Q}_2^2)$$
$$+ \mu_3^*\hat{Q}_1\hat{Q}_2 + \mu_4(\hat{Q}_1 + \hat{Q}_2)\hat{Q}_3 + \frac{1}{2!}\mu_5\hat{Q}_3^2$$
$$+ \frac{1}{3!}\mu_6(\hat{Q}_1^3 + \hat{Q}_2^3) + \frac{1}{2!}\mu_6^*\hat{Q}_1\hat{Q}_2(\hat{Q}_1 + \hat{Q}_2)$$
$$+ \frac{1}{2!}\mu_7(\hat{Q}_1^2 + \hat{Q}_2^2)\hat{Q}_3 + \mu_7^*\hat{Q}_1\hat{Q}_2\hat{Q}_3$$
$$+ \frac{1}{2!}\mu_8(\hat{Q}_1 + \hat{Q}_2)\hat{Q}_3^2 + \frac{1}{3!}\mu_{10}^*\hat{Q}_1\hat{Q}_2(\hat{Q}_1^2 + \hat{Q}_2^2)$$
$$+ \frac{1}{2!2!}\mu_{10}^{**}\hat{Q}_1^2\hat{Q}_2^2 + \frac{1}{3!}\mu_{11}(\hat{Q}_1^3 + \hat{Q}_2^3)\hat{Q}_3$$
$$+ \frac{1}{2!}\mu_{11}^*\hat{Q}_1\hat{Q}_2(\hat{Q}_1 + \hat{Q}_2)\hat{Q}_3 + \frac{1}{2!2!}\mu_{12}(\hat{Q}_1^2 + \hat{Q}_2^2)$$
$$\hat{Q}_3^2 + \frac{1}{2!}\mu_{12}^*\hat{Q}_1\hat{Q}_2\hat{Q}_3^2 \tag{23}$$

Whereas the dipole form in ref 31 (eq 20) uses a normal mode expansion of the linear part and an empirical parametrization of the nonlinear part, the current work expands the full dipole operator in the normal modes to 4th order. As a result, the parameters of the current model are associated with the partial derivatives of $\hat{M}$ with respect to the $\hat{Q}_i$. We express the nth power of $\hat{Q}_i$ as creation-annihilation n-tuples

$$\hat{Q}_i^{\,n} = \hat{a}_i^{\dagger n} + \sum_{\text{perm}} \hat{a}_i^{\dagger(n-1)}\hat{a}_i + \sum_{\text{perm}} \hat{a}_i^{\dagger(n-2)}\hat{a}_i^2 +$$
$$\dots + \sum_{\text{perm}} \hat{a}_i^{\dagger 2}\hat{a}_i^{(n-2)} + \sum_{\text{perm}} \hat{a}_i^{\dagger}\hat{a}_i^{(n-1)} + \hat{a}_i^{n} \tag{24}$$

and we keep only the pure creation (first term) and pure annihilation (last term); all other terms account for transitions involving less than n quanta. We then integrate eq 23 in the $|Q_1Q_2Q_3\rangle$ basis and obtain the model illustrated in Figure 3d. The polarizability operator is parametrized in a similar way; however, it is only expanded to second power in Q_i, since the final Raman interaction is expected to be linear.[31]

To fit the simulated RDM spectrum to the experimental TTR result, we keep $\hbar\omega_1$, $\hbar\omega_3$, μ_1, μ_3, and α_1 fixed, while varying the remaining parameters. We perform the RDM dynamics in the diagonal representation of the Hamiltonian. As such, we diagonalize H

$$H' = D^\dagger H D \tag{25}$$

and apply the same transformation to the dipole and polarizability

$$M' = D^\dagger M D, \quad \Pi' = D^\dagger \Pi D \tag{26}$$

performing the RDM simulations with H', M', and P'.

3. RESULTS AND DISCUSSIONS

The results are presented in two parts. We first present the revised experimental spectrum obtained through the transformation of the time coordinates. We then discuss the results of the RDM model introduced in this work.

3.1. Revised Experimental Spectrum. The raw experimental TTR response is comprised of an orientational molecular response with superimposed oscillations arising from vibrational coherences. As in previous work,[27,30] we focus on the vibrational component of the response, so we use an exponential fit along t_2 to detrend the orientational response from the data.

In Figure 4a−c, we demonstrate how the vibrational signal changes upon application of the time-coordinate transformation from section 2.1. The first step of the transformation involves a skew along t_2, which makes the response function appear symmetric with respect to the $t_1 = 0$ line. The transformed signal is symmetric because swapping the order of the THz pulses does not change the response type; in both cases, we measure a TTR signal. This is unlike a TRT experiment where inverting the pulse order results in a RTT sequence which measures a different correlation function altogether.[23] The second time transformation involves a flip with respect to t_1, which, due to the symmetry of the response about $t_1 = 0$, simply averages the A and B regions of the data and improves the signal-to-noise ratio.

Panels d and e of Figure 4 show the absolute value Fourier transforms of the original and transformed time responses, respectively. The revised spectrum is significantly simplified (panel e). Whereas the original spectrum features six intense peaks, the revised spectrum shows three features that are familiar in the context of conventional two-dimensional spectroscopy. The most intense peak forms at $f_1 = \omega_3 - \omega_1$ and reports on the coupling between modes Q_1 and Q_3 via a nonlinear dipole interaction. The equivalent mode in the negative $f_2 < 0$ quadrant is closely related and shows a clear rephasing pathway. Note that in the revised spectrum, the $f_2 < 0$ quadrant corresponds to true rephasing, whereas in the original spectrum the peaks involve a mix of rephasing and higher overtone nonrephasing pathways. Interestingly, the most intense true-rephasing feature appears tilted at an angle; this tilt could be related to the degree of inhomogeneous broadening. Finally, in the nonrephasing quadrant along the first diagonal, the higher frequency features appear symmetric to those at lower frequency.

3.2. Parameterization of the RDM Model. We fit the parameters of the RDM model with respect to the revised experimental spectrum using the Levenberg−Marquardt algorithm implemented in Octave,[54−56] minimizing the penalty function in eq 8. For each value of the regularization parameter λ, we start with random initial guesses for the RDM parameters, sampled uniformly from the $[−1, 1]$ interval. The fitting problem is highly under-determined, featuring multiple local minima, due to the large number (order 10^4) of Liouville paths that compete in the creation of a relatively small number of peaks. Additionally, the dipole and polarizability parameters can take negative values, which lead to peak cancellations. To address these challenges, we perform multiple minimizations, starting each time from a different random initial guess.

In Figure 5a, we plot all the converged solutions as a function of the maximum fitted parameter $\max(h_i, \mu_j, \alpha_k)$, and color them according to the L_2 regularization strength, λ. Clustered to the left are under-fitted results with small fitting parameters but large errors, while to the right are the overfitted results that match the

spectrum at the expense of unphysical parameters. The optimal solution lies in the intermediate regime with $\lambda = 100$, as indicated in Figure 5a. Three independent minimizations starting from different initial guesses converged to the same error with very similar parameters, suggesting relative robustness of this optimal paremeterization. We summarize the best-fit parameters in Tables 1 and 2, which report the values of the transition dipole elements, and we show the full transition dipole matrix in Figure 5b.

Table 1. Values of the Transition Dipole Matrix, Obtained from Ab Initio (CCSD/aug-cc-pVTZ) Calculations[31] and via Fitting of the RDM Models in Ref [31] and in the Current Work

$\langle i|\hat{M}|j\rangle$	no. Q	CCSD[31]	RDM (ref [31])	RDM (current)
$\|000\rangle \rightarrow \|100\rangle$	1	1.00	1.00 (fixed)	1.00 (fixed)
$\|000\rangle \rightarrow \|001\rangle$	1	1.01	1.60 (fixed)	1.60 (fixed)
$\|100\rangle \rightarrow \|001\rangle$	2	0.04	$0.009(\mu_4)$	$0.000\,(\mu_4)$
$\|200\rangle \rightarrow \|101\rangle$	2	0.06	$0.000(\mu_4')$	$0.000\,(\sqrt{2}\,\mu_4)$
$\|101\rangle \rightarrow \|002\rangle$	2	0.06	$0.000(\mu_4'')$	$0.000\,(\sqrt{2}\,\mu_4)$
$\|100\rangle \rightarrow \|002\rangle$	3	0.00	$0.364(\mu_8)$	$-0.014\left(\frac{\sqrt{2}}{2}\mu_8\right)$
$\|001\rangle \rightarrow \|200\rangle$	3	0.01	$0.442(\mu_7)$	$0.013\left(\frac{\sqrt{2}}{2}\mu_7\right)$
$\|101\rangle \rightarrow \|300\rangle$	3	0.02	$0.034(\mu_7')$	$0.023\left(\frac{\sqrt{6}}{2}\mu_7\right)$
$\|001\rangle \rightarrow \|300\rangle$	4		$0.023(\mu_{11})$	$0.000\left(\frac{\sqrt{6}}{6}\mu_{11}\right)$
$\|200\rangle \rightarrow \|002\rangle$	4		$0.092(\mu_{12})$	$-0.005\,(1/2\,\mu_{12})$

Table 2. Hamiltonian and Transition Polarizability Parameters of the RDM Model

$\hbar\omega_1$	4.7 (fixed)	$\hbar\omega_3$	6.6 (fixed)
$\Delta_1/\hbar\omega_1$	−0.52%	$\Delta_3/\hbar\omega_3$	−0.10%
$\beta_{12}/\hbar\omega_1$	−0.05%	$\beta_{13}/\hbar\omega_3$	+0.14%
α_1	1.00 (fixed)	α_2	−0.003

The resulting RDM simulated spectrum shown in Figure 5c is in excellent agreement with the revised experimental spectrum (Figure 4e). This can be clearly seen in Figure 5d, which provides a side-by-side comparison between simulation and experiment along the three most important 1D traces from the 2D response.

It is found that use of the experimental pulse shape $E_T(t)$ in the RDM simulations is crucial for reproducing the experimental spectrum. Using simple δ-functions to simulate the response, otherwise with the same RDM parameters, gives a radically different result, with just one dominant peak on the diagonal at $f_2 = 4.7$ THz.

The dipole nonlinearities fitted with the RDM model in this work are significantly smaller than those found in ref [31], and they agree well with results from ab initio electronic structure calculations (see Table 1). Critically, the third-order fitted nonlinearities in the current RDM model have the same order of magnitude as those from the ab initio electronic structure calculations, in contrast with the third-order terms from the fitted RDM model of ref [31]. This central result demonstrates that the refined treatment of the RDM model and the experimental spectrum in the current work removes the central inconsistency of ref [31]. Likewise, the fourth-order terms in the fitted RMD model of the current work are vastly smaller than those that were necessarily invoked in the previous study.[31] For the second-order terms, both the current and earlier RDM

Panel (b) transition dipole matrix $\hat{M}$:

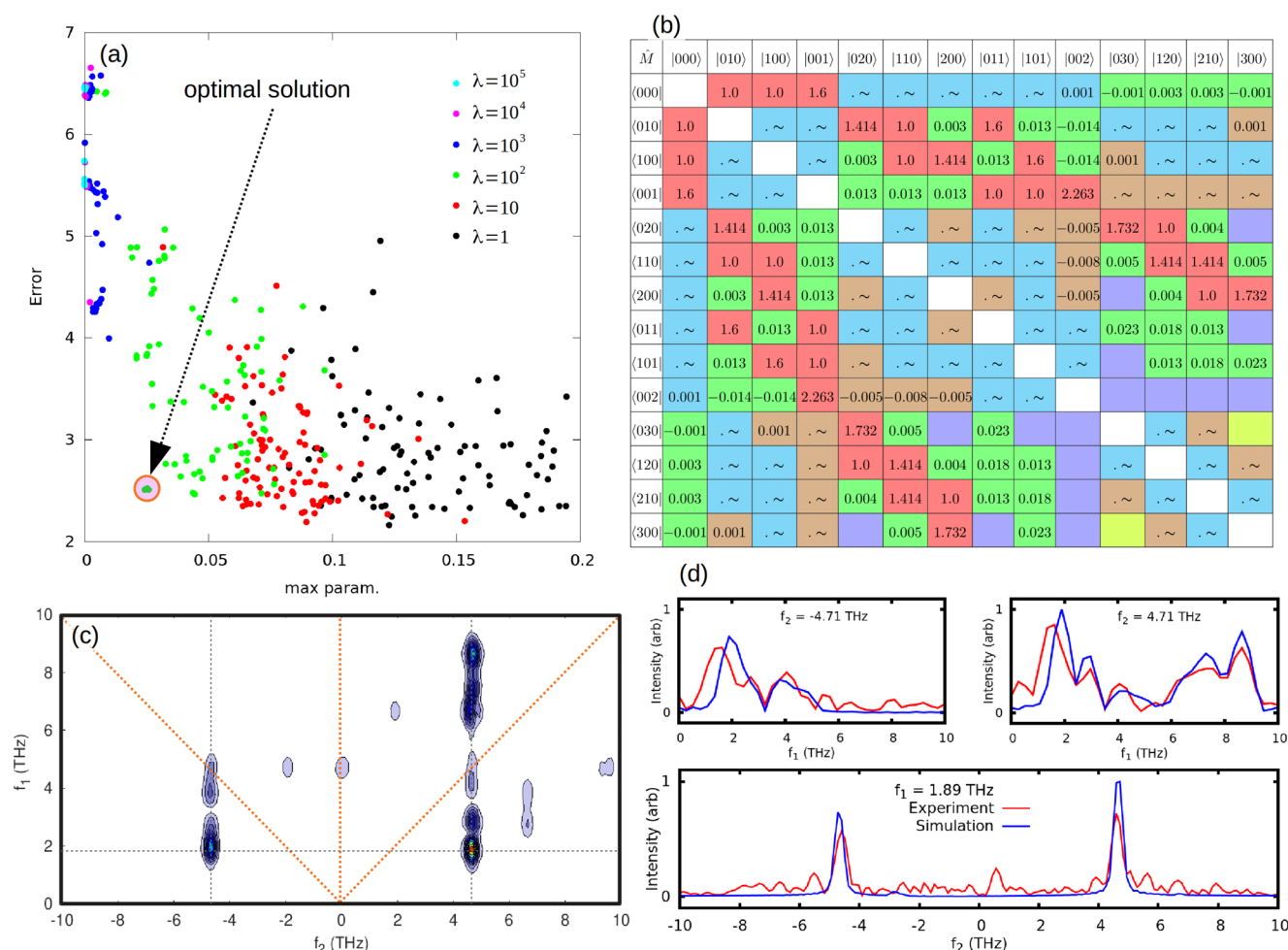| $\hat{M}$	$|000\rangle$	$|010\rangle$	$|100\rangle$	$|001\rangle$	$|020\rangle$	$|110\rangle$	$|200\rangle$	$|011\rangle$	$|101\rangle$	$|002\rangle$	$|030\rangle$	$|120\rangle$	$|210\rangle$	$|300\rangle$
$\langle 000|$		1.0	1.0	1.6	.~	.~	.~	.~	.~	0.001	−0.001	0.003	0.003	−0.001
$\langle 010|$	1.0		.~	.~	1.414	1.0	0.003	1.6	0.013	−0.014	.~	.~	.~	0.001
$\langle 100|$	1.0	.~		.~	0.003	1.0	1.414	0.013	1.6	−0.014	0.001	.~	.~	.~
$\langle 001|$	1.6	.~	.~		0.013	0.013	0.013	1.0	1.0	2.263	.~	.~	.~	.~
$\langle 020|$	.~	1.414	0.003	0.013		.~	.~	.~	.~	−0.005	1.732	1.0	0.004	
$\langle 110|$	.~	1.0	1.0	0.013	.~		.~	.~	.~	−0.008	0.005	1.414	1.414	0.005
$\langle 200|$	.~	0.003	1.414	0.013	.~	.~		.~	.~	−0.005		0.004	1.0	1.732
$\langle 011|$	.~	1.6	0.013	1.0	.~	.~	.~		.~	.~	0.023	0.018	0.013	
$\langle 101|$	.~	0.013	1.6	1.0	.~	.~	.~	.~		.~	0.013	0.018	0.023	
$\langle 002|$	0.001	−0.014	−0.014	2.263	−0.005	−0.008	−0.005	.~	.~					
$\langle 030|$	−0.001	.~	0.001	.~	1.732	0.005		0.023				.~	.~	
$\langle 120|$	0.003	.~	.~	.~	1.0	1.414	0.004	0.018	0.013		.~		.~	.~
$\langle 210|$	0.003	.~	.~	.~	0.004	1.414	1.0	0.013	0.018		.~	.~		.~
$\langle 300|$	−0.001	0.001	.~	.~		0.005	1.732		0.023			.~	.~	

Figure 5. Fitting the parameters of the RDM model to experiment. Panel a illustrates the regularization procedure. Each point is a local solution represented by a set of fitted parameters p_i. Here we plot the error of each solution ΔE_i as a function of the maximum parameter value, $\max(p_i)$. The color represents the different regularization coefficient λ. The optimal solution minimizes the error with the smallest possible parameters. Panels b and c show the transition dipole matrix, the simulated spectrum corresponding to the optimal solution identified in panel a. In panel b, we use the placeholder " ~ " for parameters that are essentially zero within three significant digits. Panel d shows three important 1D slices through the 2D spectrum at $f_1 = 1.89$ THz and $f_2 = +-$ 4.71 THz to facilitate the comparison to the experimental result. The fit was performed with respect to the revised experimental spectrum shown in Figure 4d.

models have very small fitted values. It is found that the difference between the fitted and ab initio values for the second-order terms is insignificant. We confirmed this by running the current RDM model with the ab initio values for μ_4 and all other fitted parameters unchanged and finding that the resulting simulated spectrum is unaffected.

Finally, in Table 2, we report the fitted RDM values for the anharmonicity Δ_i of the normal modes, their mechanical coupling β_{ij}, and the first order polarizability elements α_1 and α_2. We find small anharmonicities and mechanical coupling elements, which points to relatively harmonic, weakly coupled normal modes in bromoform. This conclusion is in agreement with vibrational second-order perturbation theory (VPT2) calculations performed previously.[31] Finally, the polarizability matrix elements obtained in this current work are in good agreement with those obtained in our previous work,[31] with very small nonlinear elements indicating that the final Raman interaction is indeed a linear process.

It is worth noting that the simulated spectrum has low-intensity peaks at $f_2 \simeq 6.6$ THz that bear resemblance to those in the experimental spectrum. Given the weakness of these peaks, they make a small contribution to the error function in the fitting and are thus poorly resolved. Additionally, in some fits, we found that the features at $f_2 \simeq 5.5$ THz might be connected to the mechanical coupling between $Q_{1,2}$ and Q_3. Future refinement of the RDM model and higher resolution experiments are needed to interpret these subtle features.

4. CONCLUSIONS

Our original TTR study of bromoform[31] revealed large dipole nonlinearities which were inconsistent with ab initio electronic structure calculations. Here, we refine both the experimental and theoretical description of this system, resolving the inconsistency. The key refinements are described below.

First, we revised the experimental spectrum by introducing a simplifying time-coordinate transformation. Because of the symmetry of the experimental setup, the time response must be skewed and flipped before taking the Fourier transform to enable correct interpretation. The new spectrum reveals fewer features and true rephasing signals which are symmetric with their nonrephasing counterparts, as expected.

Second, we have developed an RDM model that analytically includes all dipole and polarizability matrix elements up to 4th

order. We also include mechanical anharmonicity and mode-coupling in the model Hamiltonian. This refined RDM model preserves the symmetry of the bromoform molecule.

Lastly, we rigorously account for the inversion symmetry of the liquid by excluding even-order field interactions from the response. We achieve this by simulating the response of the system to both positive and negative THz fields and combining the two results. The final response is cubic in the field, in agreement with the experimentally measured TTR response.

The revised experimental spectrum is used to fit the parameters of the updated RDM model, leading to good agreement. The fitted nonlinearities are orders of magnitude smaller than found in our previous work and agree well with ab initio electronic structure calculations. Regardless, the original conclusion that nonlinearities in the dipole surface of the intramolecular vibrations drive the TTR response of bromoform remains unchanged.

■ AUTHOR INFORMATION

Corresponding Authors
*E-mail: gab@gps.caltech.edu.
*E-mail: tfm@caltech.edu.

ORCID ⓘ
Thomas F. Miller, III: 0000-0002-1882-5380

Notes
The authors declare no competing financial interest.

■ REFERENCES

(1) Fecko, C. J.; Eaves, J. D.; Loparo, J. J.; Tokmakoff, A.; Geissler, P. L. Ultrafast hydrogen-bond dynamics in the infrared spectroscopy of water. *Science* **2003**, *301*, 1698−1702.

(2) Zheng, J.; Kwak, K.; Fayer, M. D. Ultrafast 2D IR vibrational echo spectroscopy. *Acc. Chem. Res.* **2007**, *40*, 75−83.

(3) Park, S.; Fayer, M. D. Hydrogen bond dynamics in aqueous NaBr solutions. *Proc. Natl. Acad. Sci. U. S. A.* **2007**, *104*, 16731−16738.

(4) Ramasesha, K.; De Marco, L.; Mandal, A.; Tokmakoff, A. Water vibrations have strongly mixed intra- and intermolecular character. *Nat. Chem.* **2013**, *5*, 935.

(5) Thämer, M.; De Marco, L.; Ramasesha, K.; Mandal, A.; Tokmakoff, A. Ultrafast 2D IR spectroscopy of the excess proton in liquid water. *Science* **2015**, *350*, 78−82.

(6) Dahms, F.; Fingerhut, B. P.; Nibbering, E. T.; Pines, E.; Elsaesser, T. Large-amplitude transfer motion of hydrated excess protons mapped by ultrafast 2D IR spectroscopy. *Science* **2017**, *357*, 491−495.

(7) Shim, S.-H.; Gupta, R.; Ling, Y. L.; Strasfeld, D. B.; Raleigh, D. P.; Zanni, M. T. Two-dimensional IR spectroscopy and isotope labeling defines the pathway of amyloid formation with residue-specific resolution. *Proc. Natl. Acad. Sci. U. S. A.* **2009**, *106*, 6614−6619.

(8) Bagchi, S.; Boxer, S. G.; Fayer, M. D. Ribonuclease S dynamics measured using a nitrile label with 2D IR vibrational echo spectroscopy. *J. Phys. Chem. B* **2012**, *116*, 4034−4042.

(9) Kratochvil, H. T.; Carr, J. K.; Matulef, K.; Annen, A. W.; Li, H.; Maj, M.; Ostmeyer, J.; Serrano, A. L.; Raghuraman, H.; Moran, S. D.; et al. Instantaneous ion configurations in the K+ ion channel selectivity filter revealed by 2D IR spectroscopy. *Science* **2016**, *353*, 1040−1044.

(10) Heugen, U.; Schwaab, G.; Bründermann, E.; Heyden, M.; Yu, X.; Leitner, D.; Havenith, M. Solute-induced retardation of water dynamics probed directly by terahertz spectroscopy. *Proc. Natl. Acad. Sci. U. S. A.* **2006**, *103*, 12301−12306.

(11) Heisler, I. A.; Mazur, K.; Meech, S. R. Low-frequency modes of aqueous alkali halide solutions: An ultrafast optical Kerr effect study. *J. Phys. Chem. B* **2011**, *115*, 1863−1873.

(12) Shalit, A.; Ahmed, S.; Savolainen, J.; Hamm, P. Terahertz echoes reveal the inhomogeneity of aqueous salt solutions. *Nat. Chem.* **2017**, *9*, 273.

(13) Xu, J.; Plaxco, K. W.; Allen, S. J. Probing the collective vibrational dynamics of a protein in liquid water by terahertz absorption spectroscopy. *Protein Sci.* **2006**, *15*, 1175−1181.

(14) González-Jiménez, M.; Ramakrishnan, G.; Harwood, T.; Lapthorn, A. J.; Kelly, S. M.; Ellis, E.; Wynne, K. Observation of coherent delocalised phonon-like modes in DNA under physiological conditions. *Nat. Commun.* **2016**, *7*, 11799.

(15) Turton, D. A.; Senn, H. M.; Harwood, T.; Lapthorn, A. J.; Ellis, E. M.; Wynne, K. Terahertz underdamped vibrational motion governs protein-ligand binding in solution. *Nat. Commun.* **2014**, *5*, 3999.

(16) Tokmakoff, A.; Lang, M.; Larsen, D.; Fleming, G.; Chernyak, V.; Mukamel, S. Two-Dimensional Raman Spectroscopy of Vibrational Interactions in Liquids. *Phys. Rev. Lett.* **1997**, *79*, 2702−2705.

(17) Blank, D. A.; Kaufman, L. J.; Fleming, G. R. Fifth-order two-dimensional Raman spectra of CS2 are dominated by third-order cascades. *J. Chem. Phys.* **1999**, *111*, 3105−3114.

(18) Kaufman, L. J.; Heo, J.; Ziegler, L. D.; Fleming, G. R. Heterodyne-detected fifth-order nonresonant Raman scattering from room temperature CS2. *Phys. Rev. Lett.* **2002**, *88*, 207402.

(19) Kubarych, K. J.; Milne, C. J.; Lin, S.; Astinov, V.; Miller, R. J. D. Diffractive optics-based six-wave mixing: Heterodyne detection of the full chi((5)) tensor of liquid CS2. *J. Chem. Phys.* **2002**, *116*, 2016−2042.

(20) Marder, S. R.; Perry, J. W.; Schaefer, W. P. Synthesis of organic salts with large second-order optical nonlinearities. *Science* **1989**, *245*, 626−628.

(21) Schneider, A.; Neis, M.; Stillhart, M.; Ruiz, B.; Khan, R. U. A.; Günter, P. Generation of terahertz pulses through optical rectification in organic DAST crystals: theory and experiment. *J. Opt. Soc. Am. B* **2006**, *23*, 1822.

(22) Lu, J.; Li, X.; Zhang, Y.; Hwang, H. Y.; Ofori-Okai, B. K.; Nelson, K. A. *Multidimensional Time-Resolved Spectroscopy*; Springer, 2019; pp 275−320.

(23) Savolainen, J.; Ahmed, S.; Hamm, P. Two-dimensional Raman-terahertz spectroscopy of water. *Proc. Natl. Acad. Sci. U. S. A.* **2013**, *110*, 20402−20407.

(24) Hamm, P.; Shalit, A. Perspective: Echoes in 2D-Raman-THz spectroscopy. *J. Chem. Phys.* **2017**, *146*, 130901.

(25) Berger, A.; Ciardi, G.; Sidler, D.; Hamm, P.; Shalit, A. Impact of nuclear quantum effects on the structural inhomogeneity of liquid water. *Proc. Natl. Acad. Sci. U. S. A.* **2019**, *116*, 2458−2463.

(26) Hoffmann, M. C.; Brandt, N. C.; Hwang, H. Y.; Yeh, K. L.; Nelson, K. A. Terahertz Kerr effect. *Appl. Phys. Lett.* **2009**, *95*, 231105.

(27) Allodi, M. A.; Finneran, I. A.; Blake, G. A. Nonlinear terahertz coherent excitation of vibrational modes of liquids. *J. Chem. Phys.* **2015**, *143*, 234204.

(28) Sajadi, M.; Wolf, M.; Kampfrath, T. Transient birefringence of liquids induced by terahertz electric-field torque on permanent molecular dipoles. *Nat. Commun.* **2017**, *8*, 14963.

(29) Zalden, P.; Song, L.; Wu, X.; Huang, H.; Ahr, F.; Mücke, O. D.; Reichert, J.; Thorwart, M.; Mishra, P. K.; Welsch, R.; et al. Molecular polarizability anisotropy of liquid water revealed by terahertz-induced transient orientation. *Nat. Commun.* **2018**, *9*, 2142.

(30) Finneran, I. A.; Welsch, R.; Allodi, M. A.; Miller, T. F.; Blake, G. A. Coherent two-dimensional terahertz-terahertz-Raman spectroscopy. *Proc. Natl. Acad. Sci. U. S. A.* **2016**, *113*, 6857−6861.

(31) Finneran, I. A.; Welsch, R.; Allodi, M. A.; Miller, T. F.; Blake, G. A. 2D THz-THz-Raman Photon-Echo Spectroscopy of Molecular Vibrations in Liquid Bromoform. *J. Phys. Chem. Lett.* **2017**, *8*, 4640−4644.

(32) Ciardi, G.; Berger, A.; Hamm, P.; Shalit, A. Signatures of Intra-/Intermolecular Vibrational Coupling in Halogenated Liquids Revealed by 2D Raman-THz Spectroscopy. *J. Phys. Chem. Lett.* **2019**, 4463.

(33) Teixeira-Dias, J. The Raman spectra of bromoform. *Spectrochim. Acta, Part A* **1979**, *35*, 857−859.

(34) Steffen, T.; Fourkas, J. T.; Duppen, K. Time resolved four-and six-wave mixing in liquids. I. Theory. *J. Chem. Phys.* **1996**, *105*, 7364−7382.

(35) Steffen, T.; Duppen, K. Population relaxation and non-Markovian frequency fluctuations in third-and fifth-order Raman scattering. *Chem. Phys.* **1998**, *233*, 267−285.

(36) Okumura, K.; Tanimura, Y. Energy-level diagrams and their contribution to fifth-order Raman and second-order infrared responses: Distinction between relaxation models by two-dimensional spectroscopy. *J. Phys. Chem. A* **2003**, *107*, 8092−8105.

(37) Hasegawa, T.; Tanimura, Y. Calculating fifth-order Raman signals for various molecular liquids by equilibrium and nonequilibrium hybrid molecular dynamics simulation algorithms. *J. Chem. Phys.* **2006**, *125*, 074512.

(38) Tanimura, Y.; Ishizaki, A. Modeling, Calculating, and Analyzing Multidimensional Vibrational Spectroscopies. *Acc. Chem. Res.* **2009**, *42*, 1270−1279.

(39) Hamm, P.; Savolainen, J. Two-dimensional-Raman-terahertz spectroscopy of water: Theory. *J. Chem. Phys.* **2012**, *136*, 094516.

(40) Hamm, P.; Savolainen, J.; Ono, J.; Tanimura, Y. Note: Inverted time-ordering in two-dimensional-Raman-terahertz spectroscopy of water. *J. Chem. Phys.* **2012**, *136*, 236101.

(41) Hamm, P. 2D-Raman-THz spectroscopy: A sensitive test of polarizable water models. *J. Chem. Phys.* **2014**, *141*, 184201.

(42) Ito, H.; Hasegawa, T.; Tanimura, Y. Calculating two-dimensional THz-Raman-THz and Raman-THz-THz signals for various molecular liquids: The samplers. *J. Chem. Phys.* **2014**, *141*, 124503.

(43) Ito, H.; Jo, J. Y.; Tanimura, Y. Notes on simulating two-dimensional Raman and terahertz-Raman signals with a full molecular dynamics simulation approach. *Struct. Dyn.* **2015**, *2*, 054102.

(44) Ikeda, T.; Ito, H.; Tanimura, Y. Analysis of 2D THz-Raman spectroscopy using a non-Markovian Brownian oscillator model with nonlinear system-bath interactions. *J. Chem. Phys.* **2015**, *142*, 212421.

(45) Jo, J. Y.; Ito, H.; Tanimura, Y. Full molecular dynamics simulations of liquid water and carbon tetrachloride for two-dimensional Raman spectroscopy in the frequency domain. *Chem. Phys.* **2016**, *481*, 245−249.

(46) Ito, H.; Hasegawa, T.; Tanimura, Y. Effects of Intermolecular Charge Transfer in Liquid Water on Raman Spectra. *J. Phys. Chem. Lett.* **2016**, *7*, 4147−4151.

(47) Ito, H.; Tanimura, Y. Simulating two-dimensional infrared-Raman and Raman spectroscopies for intermolecular and intramolecular modes of liquid water. *J. Chem. Phys.* **2016**, *144*, 074201.

(48) Sidler, D.; Hamm, P. Feynman diagram description of 2D-Raman-THz spectroscopy applied to water. *J. Chem. Phys.* **2019**, *150*, 044202.

(49) Hamm, P.; Zanni, M. *Concepts and Methods of 2D Infrared Spectroscopy*; Cambridge University Press, 2011.

(50) Steffen, T.; Tanimura, Y. Two-dimensional spectroscopy for harmonic vibrational modes with nonlinear system-bath interactions. I. Gaussian-white case. *J. Phys. Soc. Jpn.* **2000**, *69*, 3115−3132.

(51) Tanimura, Y.; Steffen, T. Two-dimensional spectroscopy for harmonic vibrational modes with nonlinear system-bath interactions. II. Gaussian-Markovian case. *J. Phys. Soc. Jpn.* **2000**, *69*, 4095−4106.

(52) Ishizaki, A.; Tanimura, Y. Modeling vibrational dephasing and energy relaxation of intramolecular anharmonic modes for multidimensional infrared spectroscopies. *J. Chem. Phys.* **2006**, *125*, 084501.

(53) Fernández-Liencres, M. P.; Navarro, A.; López, J. J.; Fernández, M.; Szalay, V.; de los Arcos, T.; Garcia-Ramos, J. V.; Escribano, R. M. The force field of bromoform: A theoretical and experimental investigation. *J. Phys. Chem.* **1996**, *100*, 16058−16065.

(54) Levenberg, K. A method for the solution of certain non-linear problems in least squares. *Q. Appl. Math.* **1944**, *2*, 164−168.

(55) Marquardt, D. W. An algorithm for least-squares estimation of nonlinear parameters. *J. Soc. Ind. Appl. Math.* **1963**, *11*, 431−441.

(56) Eaton, J. W.; Bateman, D.; Hauberg, S.; Wehbring, R. *GNU Octave Version 4.2.0 Manual: A High-Level Interactive Language for Numerical Computations*, 2016.